AGU PUBLICATIONS

Geophysical Research Letters

RESEARCH LETTER
10.1002/2016GL068796

Key Points:
- The data presented show that tsunamis can potentially create currents disproportionally larger than the amplitude or what scaling suggests
- Tsunami flow features, such as transitional jets and coherent structures, amplify the current magnitude near coastline discontinuities
- Forecasts of vortical motions should augment operational tsunami warnings, in addition to the standard forecasts of maximal elevations

Supporting Information:
- Supporting Information S1
- Movie S1

Correspondence to:
N. Kalligeris,
kalliger@usc.edu

Citation:
Kalligeris, N., V. Skanavis, S. Tavakkol, A. Ayca, H. El Safty, P. Lynett, and C. Synolakis (2016), Lagrangian flow measurements and observations of the 2015 Chilean tsunami in Ventura, CA, *Geophys. Res. Lett.*, *43*, doi:10.1002/2016GL068796.

Received 21 MAR 2016
Accepted 26 APR 2016
Accepted article online 2 MAY 2016

Lagrangian flow measurements and observations of the 2015 Chilean tsunami in Ventura, CA

Nikos Kalligeris[1], Vassilios Skanavis[1], Sasan Tavakkol[1], Aykut Ayca[1], Hoda El Safty[1], Patrick Lynett[1], and Costas Synolakis[1,2]

[1]Department of Civil and Environmental Engineering, University of Southern California, Los Angeles, California, USA, [2]Department of Environmental Engineering, Technical University of Crete, Chania, Greece

Abstract Tsunami-induced coastal currents are spectacular examples of nonlinear and chaotic phenomena. Due to their long periods, tsunamis transport substantial energy into coastal waters, and as this energy interacts with the ubiquitous irregularity of bathymetry, shear and turbulent features appear. The oscillatory character of a tsunami wave train leads to flow reversals, which in principle can spawn persistent turbulent coherent structures (e.g., large vortices or "whirlpools") that can dominate damage and transport potential. However, no quantitative measurements exist to provide physical insight into this kind of turbulent variability, and no motion recordings are available to help elucidate how these vortical structures evolve and terminate. We report our measurements of currents in Ventura Harbor, California, generated by the 2015 Chilean *M*8.3 earthquake. We measured surface velocities using GPS drifters and image sequences of surface tracers deployed at a channel bifurcation, as the event unfolded. From the maps of the flow field, we find that a tsunami with a near-shore amplitude of 30 cm at 6 m depth produced unexpectedly large currents up to 1.5 m/s, which is a fourfold increase over what simple linear scaling would suggest. Coherent turbulent structures appear throughout the event, across a wide range of scales, often generating the greatest local currents.

1. Introduction

On 16 September 2015 an *M*8.3 (U.S. Geological Survey, USGS) earthquake struck the central coast of Chile, with its epicenter between Coquimbo and Valparaiso, 490 km north of the 2010 *M*8.8 Maule earthquake. The thrust-faulting earthquake ruptured along the subduction zone interface between the Nazca and South America plates at a relatively shallow focal depth, with the depth of the large-slip area in the range 12–33 km [*Heidarzadeh et al.*, 2015]. The shaking lasted over 2 min, a harbinger warning for evacuation in near-field coastal areas, where the tsunami waves arrived within minutes. The local emergency management was effective in disseminating information, prompting a timely evacuation. Despite the extensive flooding in hard-hit coastal areas like Coquimbo and Tongoy, the casualties from the tsunami were confined to eight [*Aránguiz et al.*, 2016]. The more energetic 2010 Maule tsunami, with run-up over 29 m in Constitución, claimed 124 lives [*Fritz et al.*, 2011].

In the far field, the West Coast and Alaska Tsunami Warning Center issued an advisory for the SW California coastline, which suggested that tsunami-induced flooding was not expected to be significant, but with potentially strong currents. Harbor closures were left at the discretion of the local harbor masters, with Orange County opting for a temporary closure of all its beaches and harbors. Ventura Harbor remained operational, yet experienced the highest-amplitude waves in California, with the tide gauge registering a peak of 34 cm above tide.

The news of the powerful earthquake initiated an effort from the authors to forecast the impact of the tsunami on the coast of California, in real time. The tsunami-inverted source of NOAA (U. Kanoglu, personal communication, 2015) was used with the ComMIT interface [*Titov et al.*, 2011] to provide an accurate estimate of the surface elevation and flow speed maps in Ventura harbor before arrival (see *Tang et al.* [2016] for more information on the tsunami forecast timeline). Motivated by a handful of visual observations and numerical simulations of complex currents in harbors [*Okal et al.*, 2006; *Lynett et al.*, 2012; *Borrero et al.*, 2015], the arrival of this low-amplitude tsunami in California allowed us to collect quantitative flow measurements with minimal risk to elucidate the complex near-shore currents. A small but increasing number of current measurements

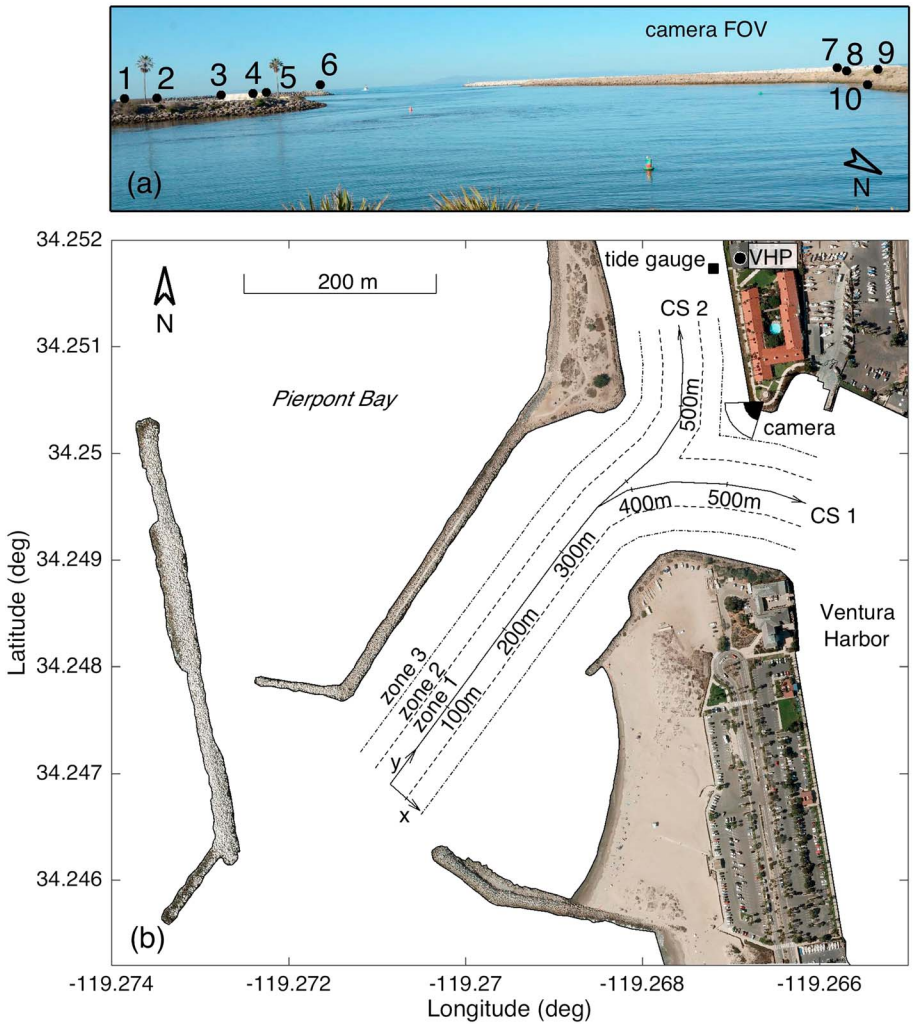

Figure 1. (a) The camera's field of view (FOV) and the ground control points used to obtain the camera's extrinsic parameters are shown in the inlet; (b) the Ventura entrance channel, camera position, and FOV, and local coordinate systems (labeled as CS 1 and CS 2). The coordinate system *y* axes are positioned in the centerline of the entrance channel and its two branches, whereas the *x* axes define the distance normal to the centerline. Three zones are defined by distance *x*: zone 1 with $|x| \leq 25$ m, zone 2 with 50 m $< |x| \leq 25$ m, and zone 3 with $|x| > 75$ m.

have been reported from acoustic current meters [*Lacy et al.*, 2012; *Borrero et al.*, 2013; *Admire et al.*, 2014] and by tracking floating debris in eyewitness videos [*Admire et al.*, 2014; *Fritz et al.*, 2012]. In contrast, here, we provide a comprehensive description of the flow field, based on a quantitative data of tsunami current effects and large-scale coherent flow structures unfolding during a real event.

2. Instrumentation

In coordination with the Ventura Harbor Patrol (VHP), we set up our instrumentation (Figure S1 in the supporting information) at 5:00 A.M. local time, 0.5 h before the arrival of the leading wave. An high-definition (HD) camera (Text S1) was positioned to continuously observe the harbor entrance channel (Figure 1) and did so for 5 h, following the arrival of the first wave. It recorded HD video at 23.97 Hz while it was dark, then switched to time-lapse mode, capturing raw frames of 4928 × 3264 resolution every 10 s.

To optically track objects in the flow, we deployed surface tracers from the deck of the VHP boat in the harbor channel. Shallow flows in rivers are known to be dominated by two-dimensional structures; hence, surface velocities are sufficient for describing the flow [*Weitbrecht et al.*, 2002]. The tracers composed of 60 cm diameter rubber balls and custom-made 40 × 40 cm styrofoam floaters. Both types of tracers were large enough

to be distinguishable in distances up to 600 m from the camera. All styrofoam floats carried flashing lights to locate them in the dark, and one also an DeLorme *InReach Explorer (DEX)* GPS unit logging at 1/2 Hz, adequate to resolve the motions of interest.

3. Methodology for Velocity Extraction

3.1. Optical Particle Tracking

Extracting velocity vectors from the surface tracers identified in the image sequence required a series of steps. We calibrated the camera in the lab to obtain the intrinsic parameters [*Bouguet*, 2015] and remove lens distortion (Text S2). We then applied the pinhole model, which relates image (p, q) to world (x, y, z) coordinates, in the form of the Direct Linear Transformation (DLT) equations [*Holland et al.*, 1997]:

$$p = \frac{xL_1 + yL_2 + zL_3 + L_4}{xL_9 + yL_{10} + zL_{11} + 1}, \quad q = \frac{xL_5 + yL_6 + zL_7 + L_8}{xL_9 + yL_{10} + zL_{11} + 1} \tag{1}$$

where $L_j, j = 1, \ldots, 11$ are the DLT coefficients. Rewriting equation (1) as a system of linear equations of the form $\mathbf{A}\cdot\vec{x} = \vec{b}$, allowed us to obtain the least squares solution of DLT coefficients (Text S3) using 10 noncoplanar ground control points (GCPs) for which the image and world coordinate pairs were obtained by a posterior survey (Figure 1a). All elevations were referenced to the mean lowest low (MLLW) datum.

Once the DLT coefficients were known, the image coordinates of the surface tracers (Text S4) could be transformed to world coordinates by rewriting equation (1) as

$$\begin{bmatrix} x \\ y \end{bmatrix} = \begin{bmatrix} [L_1 - L_9 p] & [L_2 - L_{10} p] \\ [L_5 - L_9 q] & [L_6 - L_{10} q] \end{bmatrix}^{-1} \begin{bmatrix} p - L_4 + z_t(L_{11} p - L_3) \\ q - L_8 + z_t(L_{11} q - L_7) \end{bmatrix} \tag{2}$$

where z_t is the tracer elevation, which needs to be independently estimated. z_t was set equal to the tide level above MLLW without accounting for tsunami and higher-frequency wave amplitudes. Due to the camera low view angle and the distances covered, surface elevations not accounted for, had a significant effect on the coordinate transformation. A 20 cm wave displaces the horizontal position by ≈18 m (along the line of sight) at the channel entrance. To alleviate this effect, the world coordinate pairs were transformed to polar (r, θ) with respect to the camera, and a low-pass filter with 50 s cutoff period was applied to the radial coordinate time series to filter out the high-frequency wind- and boat-generated waves (Figure S3). The filtered polar coordinates of each tracer were converted to UTM (universal transverse Mercator); then the velocities in the east and north directions were computed using the central difference scheme:

$$u_i = \frac{E_{i+1} - E_{i-1}}{t_{i+1} - t_{i-1}} \quad v_i = \frac{N_{i+1} - N_{i-1}}{t_{i+1} - t_{i-1}} \tag{3}$$

where E and N are the easting and northing UTM coordinates of the tracer, respectively, at time step i.

Finally, for each tracer, the coordinates and velocities were referenced to one of the two local coordinate systems shown in Figure 1b. The choice of local coordinate system depended on which branch each tracer would take at the channel bifurcation. The velocity pairs referenced to the local coordinate system correspond to the channel-parallel (u_y) and channel-normal velocities (u_x).

3.2. GPS

The spherical coordinate pairs extracted form the DEX GPS unit were first converted to UTM-projected coordinates, and the velocities in the east and north directions were also computed using a central difference scheme. We note that although the sampling frequency was set to 1/2 Hz, at low flow speeds the sampling frequency was automatically reduced, since the displacement within the sampling period was not sufficient to register a new point, given the accuracy of the receiver. Sudden jumps in velocity, appearing when the sampling frequency changed, were removed.

GPS receivers inherently suffer from positioning inaccuracies due to satellite- and receiver-dependent errors, ionospheric and tropospheric delays, and multipath errors [*Uren and Price*, 1994]. The absolute position error for nondifferential receivers can reach up to 3.6 m in each horizontal direction [*Johnson and Pattiaratchi*, 2004]. However, errors in velocity computation are rather affected by the relative position accuracy, namely, the temporal changes of position accuracy. The total velocity error, which is also a function of the finite differencing error, limits the motions that can be resolved. *Johnson and Pattiaratchi* [2004] have shown that the

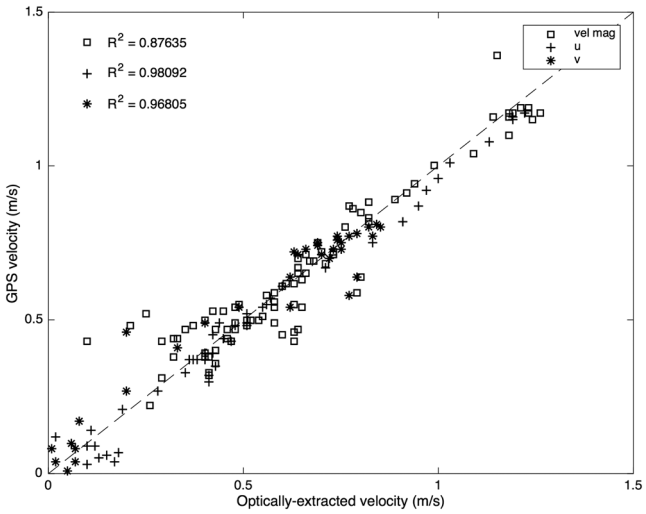

Figure 2. Scatterplot of velocities measured with the DEX GPS unit versus velocities measured optically. Squares correspond to velocity magnitude, crosses to the velocity in the eastern direction, and stars to the velocity in the north direction. The R^2 coefficients of determination are noted.

signal-to-noise ratio increases for lower frequency motions and becomes acceptable to resolve frequencies below 0.05 Hz, for 1 Hz sampling. By analogy, we low-pass filtered the velocity time series using a 0.025 Hz cut-off. The DEX floater was also traced optically, when it appeared in the camera field of view (FOV). The velocities calculated from the GPS data at those times were used to validate the optical particle tracking methodology, as shown in Figure 2.

4. Numerical Modeling

The compiled flow time histories allowed us also to evaluate the accuracy of a standard numerical model used for tsunami simulations. Given the complexity of tsunami near-shore flows, one might surmise that high-resolution and turbulence-resolving models are required to adequately describe this flow. However, uncertainties and imprecision in field-scale simulations can often obscure any such increase in modeled physics, posing the fundamental question as to whether a lower order hydrodynamic model might yield useful predictions. We used *MOST* (Method Of Splitting Tsunamis), which solves the nonlinear shallow water approximation of the parent Navier-Stokes equations, scheme [*Titov and Synolakis*, 1997], a code benchmarked with laboratory results and extensively validated operationally during tsunami events [e.g., *Titov et al.*, 2005; *Tang et al.*, 2009], but only to predict maximum inland penetration. In California, MOST has been used to produce the state's tsunami inundation maps [*Borrero et al.*, 2001; *Barberopoulou et al.*, 2011a, 2011b] and to predict currents [*Ayca et al.*, 2014]. In a recent study [*Lynett et al.*, 2014], current speeds in Crescent City, CA, during the 2011 Japan tsunami were simulated using MOST, and the comparison to estimated flow speeds at the inner harbor entrance [*Admire et al.*, 2014] was satisfactory.

Our initial conditions are derived from NOAA's (National Oceanographic and Atmospheric Administration) tsunami-inverted source (equation (S2)), as obtained using standard procedures [*Tang et al.*, 2016]. The tsunami was propagated across the Pacific Ocean using a 4 arc min grid, and in the near field through four telescopic grids of increasing resolution to reach Ventura Harbor, where 1/3 arc sec resolution was used (Text S5). The overall accuracy of the simulations was evaluated by comparing the calculated surface elevation time series at Ventura's tide gauge station with the detided recording (Figure 3e). The arrival time, phase, and amplitude of the first three waves compare well with the recording.

For our purpose, we referenced the output velocities of MOST, in the longitudinal and latitudinal directions, to the local coordinate systems defined in Figure 1b, keeping only the along-channel velocity component u_y. Instead of comparing the model results to the measurements in a Lagrangian framework, we opted to represent the model results through a mean (spatial-averaged) channel flow speed, by averaging u_y over numerical points in the harbor channel with 185 m $< y <$ 385 m (Figure S5). This representation allows for

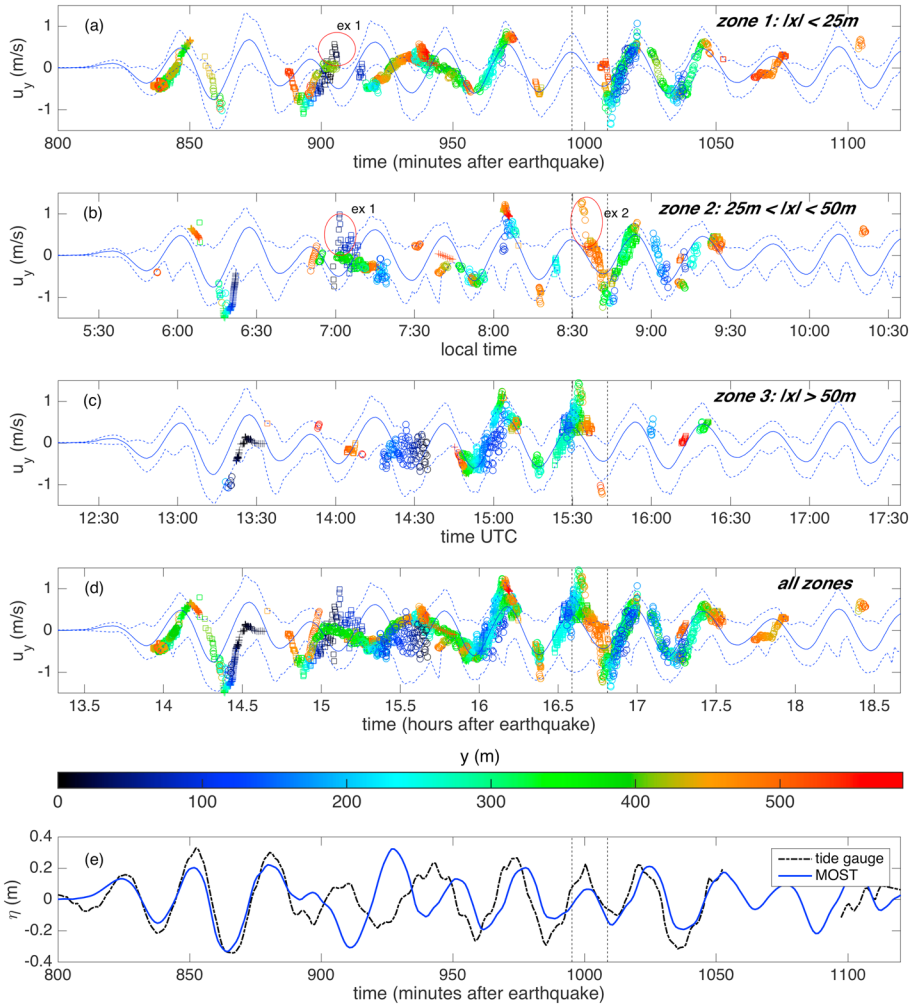

Figure 3. (a–d) Time history of channel-parallel velocity in Ventura Harbor, measured (points) versus predicted (curves). Crosses represent GPS measurements, whereas circles and squares represent optical measurements referenced to coordinate systems CS 1 and CS 2, respectively. All GPS measurements are referenced to CS 1. The flow field has been separated in three zones defined by the distance (x) normal to the channel centerline. The mean flow channel speed u_y predicted by MOST is overlaid in all subplots as continuous curves, whereas the dashed curves correspond to the minimum and maximum MOST-predicted values in each channel zone. All results are shown together in Figure 3d. Along-channel distance (y) shown with a color map. (e) Ventura's tide gauge record compared to the surface elevation time history extracted from MOST. The tide gauge record has been high-pass filtered using a cutoff period of 100 min. The location of the tide gauge is shown in Figure 1.

small-timing inaccuracies and averages out localized flow speed variations in the model. Flow speed variations are represented through the extrema across the channel length, forming a flow speed envelope.

We also used MOST to estimate the background flow due to tide by forcing the model boundaries with the predicted tidal amplitude. The simulated maximum currents in the harbor entrance channel are below 20 cm/s over three tidal cycles. During the field measurements (flood tide) they are less than 10 cm/s.

5. Results and Discussion

We summarize our quantitative results in Figure 3, which depicts the measured and predicted flow time histories across the harbor entrance channel (see Figure 4 for a top view of the tracer paths). The measurements show that the channel-parallel water flow is fluctuating with u_y velocities ranging between ±1.5 m/s. The velocity magnitude reached a maximum of 1.5 m/s at 6 m depth. These values are about four times greater than what simple scaling calculations using long-wave theory would suggest for a 30 cm wave amplitude. The MOST channel-mean speed prediction fluctuated between ±0.8 m/s, and the minimum/maximum values

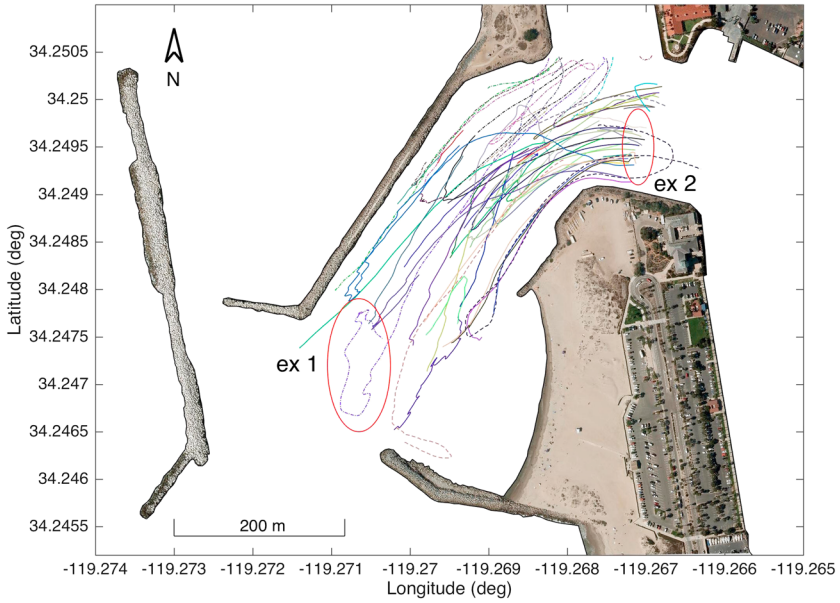

Figure 4. Projected tracer paths in the harbor entrance channel. Continuous line and dash-dotted line curves correspond to paths extracted from optical tracking, referenced to coordinate systems CS 1 and CS 2, respectively. Dashed line curves correspond to GPS tracks, all referenced to CS 1.

largely envelope the measurements. In general, the phasing matches the measurements well, with the exception of the fourth to sixth waves (6:50 to 7:40 A.M. local time). This disagreement is also evident in the tide gauge comparison and can be attributed to a range of factors, including inaccuracies in the offshore forcing [*Lynett et al.*, 2014].

We separated the flow time history in Figure 3 in three zones, defined by the distance (x) normal to the local coordinate system centerline. Zone 1 corresponds to the middle section of the harbor channel and shows the smoothest flow pattern with smaller extrema. In contrast, flows in zones 2 and 3 experience rapid acceleration/deceleration, as evident from the steep velocity gradients in the measurements. Steep velocity gradients appear when the flow in the channel starts to change direction, and vorticity is introduced from the boundaries. As examples, two tracers (labeled as *ex 1* and *ex 2*) experiencing rapid deceleration are identified in

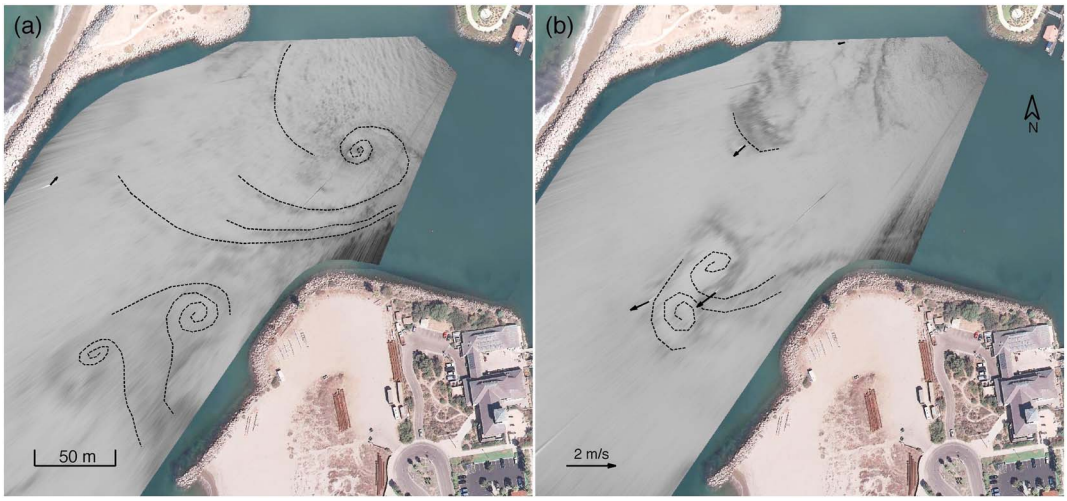

Figure 5. Rectified camera frames captured at (a) 8:29 and (b) 8:43 A.M. local time, overlaid over orthorectified USGS aerial imagery (times are shown in Figure 2 with vertical dashed lines). (a) Transitional jet and TCS forming when flow reversed toward the harbor and (b) two transitional jets expelled from the channel bifurcation corners. Vectors correspond to tracer flow speeds. TCS streamlines and the fronts of transitional jets are approximately shown with dashed curves.

Figures 3 and 4. In ex 1, the tracer decelerates rapidly during the flow reversal and is caught in a rotational structure at the entrance of the harbor channel. The second example shows a particle accelerating toward the harbor; once it turns east at the bifurcation, it enters a zone of strong turbulence adjacent to the separation region on the lee side and decelerates rapidly.

Interesting flow patterns are observed after rectifying the image sequences (see Movie S1, showing the evolution of the flow structures). Two frames captured during maximum flow speeds are shown here in Figure 5. When the flow reversed toward the harbor (positive u_y), an anticlockwise rotating turbulent coherent structure (TCS) can be identified at the bifurcation, followed by a transitional-jet dipole forming at the sharp seawall corner adjacent to the beach (Figure 5a). When the flow reversed toward offshore (negative u_y), transitional jets were expelled from the bifurcation corners, carrying three tracers that experienced surface speeds up to 1 m/s (Figure 5b). This pattern appears similar to larger tidal flows through inlets, where starting-jet and expelled boundary layer vortices form at the beginning of ebbing [*Bryant et al.*, 2012].

6. Conclusions

Our measurements of surface flows in Ventura Harbor's entrance channel during the 2015 Chilean *M*8.3 earthquake show that the surface current speeds reached 1.5 m/s in a highly turbulent, but subcritical flow. The vortical structures triggered by this tsunami persisted for over 4 h, and surface amplitudes decayed slowly. The harbor channel boundaries fed the flow with vorticity, creating transitional jets that grow in size and form coherent vortical structures [*Jirka*, 2001].

Our findings suggest that forecasts of vortical motions should augment operational tsunami warnings, in addition to the standard forecasts of maximal elevations and new forecast products which include estimates of maximal current speeds [*Wilson et al.*, 2016]. Had this 2015 tsunami been more energetic, TCS would pose a substantial navigation in the channel and for birthed vessels. As it was, the tsunami effects in Ventura Harbor existed in a scientific "Goldilocks zone," where the currents were strong enough to be unambiguously measured and of scientific relevance, but not strong enough to make navigation and field observations unsafe.

Acknowledgments
The authors acknowledge the cooperation with the Ventura Harbor Patrol, and in particular Harbor Master John Higgins, for providing assistance and access to the harbor and its equipment during the event. The authors also thank Rick Wilson of the California Geological Survey for providing contact information and tsunami event information throughout the field deployment. The authors thank an anonymous reviewer and Mohammad Heidarzadeh (University of Tokyo, Japan) for their comments on the paper. Partial funding for this effort was provided by National Science Foundation grants CMMI-1135026 and CMMI-1538624.

References

Admire, A. R., L. A. Dengler, G. B. Crawford, B. U. Uslu, J. C. Borrero, S. D. Greer, and R. I. Wilson (2014), Observed and modeled currents from the Tohoku-oki, Japan and other recent tsunamis in Northern California, *Pure Appl. Geophys.*, *171*, 3385–3403, doi:10.1007/s00024-014-0797-8.

Aránguiz, R., et al. (2016), The 16 September 2015 chile tsunami from the post-tsunami survey and numerical modeling perspectives, *Pure Appl. Geophys.*, *173*, 333–348, doi:10.1007/s00024-015-1225-4.

Ayca, A., P. Lynett, J. Borrero, K. Miller, and R. Wilson (2014), Numerical and physical modeling of localized tsunami-induced currents in harbors, *Coastal Eng. Proc.*, *1*(34), 6, doi:10.9753/icce.v34.currents.6.

Barberopoulou, A., M. R. Legg, B. Uslu, and C. E. Synolakis (2011a), Reassessing the tsunami risk in major ports and harbors of California I: San Diego, *Nat. Hazards*, *58*(1), 479–496, doi:10.1007/s11069-010-9681-8.

Barberopoulou, A., J. C. Borrero, B. Uslu, M. R. Legg, and C. E. Synolakis (2011b), A second generation of tsunami inundation maps for the state of California, *Pure Appl. Geophys.*, *168*, 2133–2146, doi:10.1007/s00024-011-0293-3.

Borrero, J. C., J. F. Dolan, and C. E. Synolakis (2001), Tsunamis within the Eastern Santa Barbara Channel, *Geophys. Res. Lett.*, *28*, 643–646, doi:10.1029/2000GL011980.

Borrero, J. C., et al. (2013), Observations, effects and real time assessment of the March 11, 2011 Tohoku-oki tsunami in New Zealand, *Pure Appl. Geophys.*, *170*, 1229–1248, doi:10.1007/s00024-012-0492-6.

Borrero, J. C., P. J. Lynett, and N. Kalligeris (2015), Tsunami currents in ports, *Philos. Trans. R. Soc. London, Ser. A*, *373*(2053), 20140372, doi:10.1098/rsta.2014.0372.

Bouguet, J.-Y. (2015), Camera calibration toolbox for Matlab. Computational Vision at the California Institute of Technology.

Bryant, D. B., K. A. Whilden, S. A. Socolofsky, and K.-A. Chang (2012), Formation of tidal starting-jet vortices through idealized barotropic inlets with finite length, *Environ. Fluid Mech.*, *12*, 301–319, doi:10.1007/s10652-012-9237-4.

Fritz, H., et al. (2011), Field survey of the 27 February 2010 Chile tsunami, *Pure Appl. Geophys.*, *168*, 1989–2010, doi:10.1007/s00024-011-0283-5.

Fritz, H. M., D. A. Phillips, A. Okayasu, T. Shimozono, H. Liu, F. Mohammed, V. Skanavis, C. E. Synolakis, and T. Takahashi (2012), The 2011 Japan tsunami current velocity measurements from survivor videos at Kesennuma Bay using LiDAR, *Geophys. Res. Lett.*, *39*, L00G23, doi:10.1029/2011GL050686.

Heidarzadeh, M., S. Murotani, K. Satake, T. Ishibe, and A. R. Gusman (2015), Source model of the 16 September 2015 Illapel, Chile, *Mw* 8.4 earthquake based on teleseismic and tsunami data, *Geophys. Res. Lett.*, *43*, 643–650, doi:10.1002/2015GL067297.

Holland, K. T., R. A. Holman, and T. C. Lippmann (1997), Practical use of video imagery in near-shore oceanographic field studies, *IEEE J. Oceanic Eng.*, *22*(1), 81–92, doi:10.1109/48.557542.

Jirka, G. H. (2001), Large scale flow structures and mixing processes in shallow flows, *J. Hydraul. Res.*, *39*(6), 567–573, doi:10.1080/00221686.2001.9628285.

Johnson, D., and C. Pattiaratchi (2004), Application, modelling and validation of surf zone drifters, *Coastal Eng.*, *51*, 455–471, doi:10.1016/j.coastaleng.2004.05.005.

Lacy, J. R., D. M. Rubin, and D. Buscombe (2012), Currents, drag, and sediment transport induced by a tsunami, *J. Geophys. Res.*, *117*, C09028, doi:10.1029/2012JC007954.

Lynett, P. J., J. C. Borrero, R. Weiss, S. Son, D. Greer, and W. Renteria (2012), Observations and modeling of tsunami-induced currents in ports and harbors, *Earth Planet. Sci. Lett.*, *327–328*, 68–74, doi:10.1016/j.epsl.2012.02.002.

Lynett, P. J., J. Borrero, S. Son, R. Wilson, and K. Miller (2014), Assessment of the tsunami-induced current hazard, *Geophys. Res. Lett.*, *41*, 2048–2055, doi:10.1002/2013GL058680.

Okal, E. A., H. M. Fritz, P. E. Raad, C. Synolakis, Y. Al-Shijbi, and M. Al-Saifi (2006), Oman field survey after the December 2004 Indian Ocean tsunami, *Earthquake Spectra*, *22*, 203–218, doi:10.1193/1.2202647.

Tang, L., V. V. Titov, and C. D. Chamberlin (2009), Development, testing, and applications of site-specific tsunami inundation models for real-time forecasting, *J. Geophys. Res.*, *114*, C12025, doi:10.1029/2009JC005476.

Tang, L., V. V. Titov, C. Moore, and Y. Wei (2016), Real-time assessment of the 16 September 2015 Chile tsunami and implications for near-field forecast, *Pure Appl. Geophys.*, *173*, 369–387, doi:10.1007/s00024-015-1226-3.

Titov, V. V., and C. E. Synolakis (1997), Extreme inundation flows during the Hokkaido-Nansei-oki tsunami, *Geophys. Res. Lett.*, *24*(11), 1315–1318, doi:10.1029/97GL01128.

Titov, V. V., F. I. Gonzalez, E. N. Bernard, M. C. Eble, H. O. Mofjeld, J. C. Newman, and A. J. Venturato (2005), Real-time tsunami forecasting: Challenges and solutions, *Nat. Hazards*, *35*(1), 35–41, doi:10.1007/s11069-004-2403-3.

Titov, V. V., C. W. Moore, D. J. M. Greenslade, C. Pattiaratchi, R. Badal, C. E. Synolakis, and U. Kanoglu (2011), A new tool for inundation modeling: Community modeling interface for tsunamis (ComMIT), *Pure Appl. Geophys.*, *168*, 2121–2131, doi:10.1007/s00024-011-0292-4.

Uren, J., and W. F. Price (1994), *Surveying for Engineers*, 3rd edn., Macmillan, Basingstoke, U. K.

Weitbrecht, V., G. Kühn, and G. H. Jirka (2002), Large scale PIV-measurements at the surface of shallow water flows, *Flow Meas. Instrum.*, *13*(5–6), 237–245, doi:10.1016/S0955-5986(02)00059-6.

Wilson, R., P. Lynett, K. Miller, A. Admire, A. Ayca, E. Curtis, L. Dengler, M. Hornick, T. Nicolini, and D. Peterson (2016), Maritime tsunami response playbooks: Background information and guidance for response and hazard mitigation use, California Geological Survey Special Report 241, p. 48.